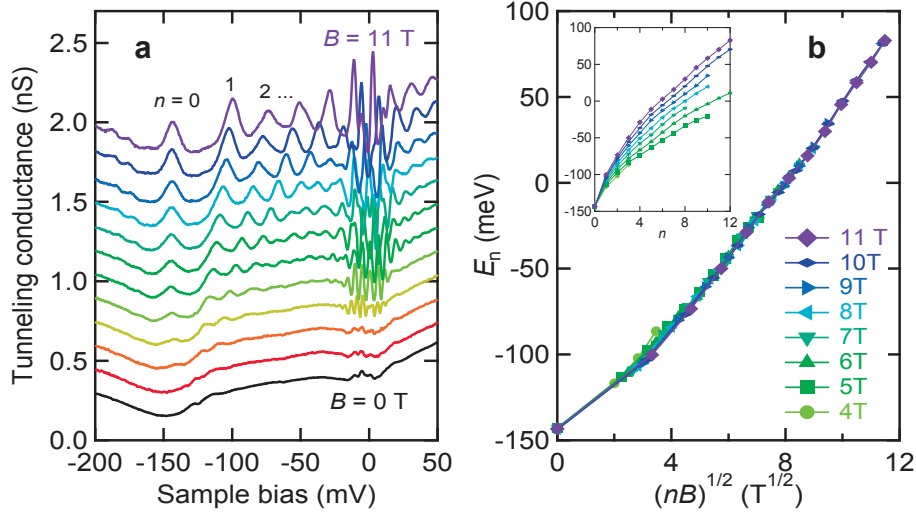# 1 Supplementary Figure

Figure S1: **Landau-level spectra showing the Dirac behavior**. **a**, Tunneling spectra taken at different B from 0 T up to 11 T with 1 T interval. Data were taken at the location 15 nm to the right from the lower left corner of Fig. 1**b-e**. Measurement conditions were $V_s = -100$ mV, $I_t = 50$ pA and $V_{\mathrm{mod}} = 1.4$ mV$_{\mathrm{rms}}$. Spectra under the fields are shifted vertically for clarity. The B-independent LL_0 guarantees that these LLs are indeed associated with the Dirac surface state. **a**, Another Dirac nature is manifested in $E_n(B)$ which are scaled by the square-roots of B and n. A finite curvature of the scaling function is due to the finite curvature of the energy-momentum dispersion relation [S1]. The inset shows the n dependence of E_n before the scaling.

2 Supplementary Notes

2.1 Model and method of calculation

We consider two models of two-dimensional (2D) electron systems; a conventional electron system with a parabolic dispersion relation and a Dirac electron system with a linear dispersion relation. In both models, we assume that a magnetic field B is applied perpendicular to the 2D plane. We introduce circular symmetric Coulomb potentials to both models, which are described in the form of

$$V(\mathbf{r}) = V(r) = -\frac{V_0 d}{\sqrt{r^2 + d^2}}, \tag{S1}$$

where r is the in-plane distance measured from the bottom of the potential. The potential simulates a situation where a charged impurity is located at a distance d below the 2D system. We neglect Coulomb interactions among electrons and the Zeeman effect.

2.1.1 Conventional electron system

First, we consider the model of the conventional electron system, following a theoretical work by Yoshioka [S2]. The model Hamiltonian is written as

$$H^{\mathrm{C}} = H_0^{\mathrm{C}} + V(\mathbf{r}), \tag{S2}$$

where

$$H_0^{\mathrm{C}} = \frac{1}{2m^*}(\mathbf{p} - e\mathbf{A})^2 = \frac{1}{2m^*}(\pi_x^2 + \pi_y^2) \tag{S3}$$

is the unperturbed Hamiltonian for the conventional 2D electron system in a magnetic field. Here, m^* and e (< 0) are the effective mass and the charge of electrons, respectively. The 2D vectors $\mathbf{p} = (p_x, p_y)$ and $\mathbf{A} = (A_x, A_y)$ represent the momentum and the vector potential, respectively. The dynamic momentum vector $\boldsymbol{\pi} = (\pi_x, \pi_y)$ is defined as $\boldsymbol{\pi} = \mathbf{p} - e\mathbf{A}$. In the presence of a uniform magnetic field B, the vector potential is given as $\mathbf{A} = (-By/2, Bx/2)$ in the symmetric gauge.

The eigenstates of H_0^{C} are well-known Landau states and the eigenenergies are quantized to Landau levels. Because $[H_0^{\mathrm{C}}, L_z] = 0$, where $L_z = (\mathbf{r} \times \mathbf{p})_z$ is the z-component of the orbital angular momentum, the eigenvalues of L_z are good quantum numbers and the energy eigenstates of H_0^{C} are simultaneous eigenstates of L_z. The eigenenergies and the eigenstates of H_0^{C} are given by

$$E_n^{\mathrm{C}} = \hbar\omega_{\mathrm{c,C}}\left(n + \frac{1}{2}\right) \tag{S4}$$

$$
\begin{aligned}
\langle \mathbf{r}|\phi_{n,l_z}\rangle &\equiv \phi_{n,l_z}(r, \theta) \\
&= \frac{1}{\sqrt{2\pi}l_B}\sqrt{\frac{N!}{(N + |l_z|)!}} \times \exp\left(-\frac{1}{4}\xi^2 + il_z\theta\right)\left(\frac{1}{\sqrt{2}}\xi\right)^{|l_z|}L_N^{|l_z|}\left(\frac{1}{2}\xi^2\right)
\end{aligned} \tag{S5}
$$

in in polar coordinates (r, θ), where $\omega_{\mathrm{c,C}} \equiv \frac{|e|B}{m^*}$ is the cyclotron frequency, $n = 0, 1, 2, \cdots$ are the Landau level indexes, $l_z\hbar = n\hbar, (n-1)\hbar, (n-2)\hbar, \cdots$ are the eigenvalues of L_z, $\xi = r/l_B$ is the radius normalized by the magnetic length $l_B \equiv \sqrt{\hbar/|e|B}$, and $N \equiv n - (l_z + |l_z|)/2$. The Larmor radii of these states are calculated as

$$\sqrt{\langle\phi_{n,l_z}|(\mathbf{r} - \mathbf{R})^2|\phi_{n,l_z}\rangle} = l_B\sqrt{(2n+1)}, \tag{S6}$$

where $\mathbf{R}$ is the centre coordinate of the cyclotron motion.

Because $V(\mathbf{r})$ is circular symmetric, $[L_z, V(\mathbf{r})] = 0$. Therefore l_z remains a good quantum number even in the presence of $V(\mathbf{r})$ and the total Hamiltonian $H^{\mathrm{C}} = H_0^{\mathrm{C}} + V(\mathbf{r})$ can be block diagonalized with respect to l_z. For a given l_z, each block Hamiltonian $H^{\mathrm{C}}(l_z)$ is written as

$$H^{\mathrm{C}}(l_z) = \sum_n |\phi_{n,l_z}\rangle\hbar\omega_{\mathrm{c,C}}\left(n + \frac{1}{2}\right)\langle\phi_{n,l_z}| + \sum_{n_1,n_2}|\phi_{n_1,l_z}\rangle\langle\phi_{n_1,l_z}|V(r)|\phi_{n_2,l_z}\rangle\langle\phi_{n_2,l_z}|. \tag{S7}$$

We calculate the eigenenergies E_{n,l_z}^{C} and the eigenstates $\Phi_{n,l_z}(r,\theta)$ for each $H^{\mathrm{C}}(l_z)$ by diagonalizing it numerically. Using the obtained E_{n,l_z}^{C} and $\Phi_{n,l_z}(r,\theta)$, we calculate the local density of states (LDOS) defined as

$$D^{\mathrm{C}}(E,\mathbf{r}) = \sum_{n,l_z} \frac{\Gamma}{(E - E_{n,l_z}^{\mathrm{C}})^2 + \Gamma^2} |\Phi_{n,l_z}(r,\theta)|^2, \tag{S8}$$

assuming that each state has a Lorentzian-shape broadening with a damping parameter Γ.

2.1.2   Dirac electron system

Next, we consider the model for the Dirac electron system. The model Hamiltonian is written as

$$H = H_0 + V(\mathbf{r})\sigma_0, \tag{S9}$$

where

$$H_0 = v(\sigma_x \pi_y - \sigma_y \pi_x) = v \begin{pmatrix} 0 & \pi_y + i\pi_x \\ \pi_y - i\pi_x & 0 \end{pmatrix} \tag{S10}$$

is the unperturbed Hamiltonian for the 2D Dirac electrons in a magnetic field. Here, v is the electron velocity, σ_0 is the (2×2) unity matrix, σ_x and σ_y are the Pauli matrices.

Unlike the conventional electron system, the unperturbed Hamiltonian H_0 does not commute with the orbital angular momentum $[H_0, L_z\sigma_0] \neq 0$. Instead H_0 commute with the z-component of the total angular momentum (J_z),

$$[H_0, J_z] = 0, \tag{S11}$$

where J_z is defined as $J_z \equiv L_z\sigma_0 + \frac{\hbar}{2}\sigma_z$. Therefore the eigenstates of H_0 can be the simultaneous eigenstates of J_z. The eigenenergies and the two-component eigenstates of H_0 are obtained in polar coordinates (r,θ) as follows:

$$E_n = \begin{cases} 0 & n = 0 \\ \mathrm{sgn}(n)\hbar\omega_{\mathrm{c}}\sqrt{|n|} & n \neq 0 \end{cases} \tag{S12}$$

$$\langle\mathbf{r}|\boldsymbol{\psi}_{n,j_z}\rangle \equiv \boldsymbol{\psi}_{n,j_z}(r,\theta) = \begin{cases} \begin{pmatrix} 0 \\ \phi_{0,l_z}(r,\theta) \end{pmatrix} & n = 0 \\ \frac{1}{\sqrt{2}} \begin{pmatrix} \mathrm{sgn}(n)\mathrm{sgn}(l_z)\phi_{|n|-1,l_z-1}(r,\theta) \\ \phi_{|n|,l_z}(r,\theta) \end{pmatrix} & n \neq 0 \end{cases} \tag{S13}$$

where $\omega_{\mathrm{c}} \equiv \sqrt{2}v/l_B$ is the cyclotron frequency of the Dirac electron system and $\phi_{|n|,l_z}(r,\theta)$ is the same function as the $|n|$-th Landau state of the conventional electron system (eq. (S5)). These energy eigenstates are the simultaneous eigenstates of J_z with eigenvalues $j_z\hbar = (l_z - \frac{1}{2})\hbar$. The Larmor radii of these states, which are different from those in the conventional electron system, are calculated as

$$\sqrt{\langle\boldsymbol{\psi}_{n,j_z}|(\mathbf{r} - \mathbf{R})^2\sigma_0|\boldsymbol{\psi}_{n,j_z}\rangle} = \begin{cases} l_B & n = 0 \\ l_B\sqrt{2|n|} & n \neq 0 \end{cases} \tag{S14}$$

Because the potential $V(\mathbf{r})$ is circular symmetric, $[J_z, V(\mathbf{r})\sigma_0] = 0$. Therefore, j_z remains a good quantum number even in the presence of $V(\mathbf{r})\sigma_0$ and the total Hamiltonian $H = H_0 + V(\mathbf{r})\sigma_0$ can be block diagonalized with respect to j_z. Similar to the conventional electron system, we calculate the eigenenergies E_{n,j_z} and eigenstates $\mathbf{\Psi}_{n,j_z}(r,\theta)$ for each block Hamiltonian by diagonalizing it numerically. Using these eigenenergies and the eigenstates, we calculate the LDOS defined as

$$D(E, \mathbf{r}) = \sum_{n,j_z} \frac{\Gamma}{(E - E_{n,j_z})^2 + \Gamma^2} |\mathbf{\Psi}_{n,j_z}(r,\theta)|^2, \tag{S15}$$

assuming a Lorentzian-shaped broadening with a damping parameter Γ.

2.2 Comparison between conventional- and Dirac-Landau levels

The calculated LDOSs for the Dirac and the conventional electron systems are shown in Figs. 4 (main text) and S1, respectively. The parameters of the potential are chosen to be $V_0 = 1.3\hbar\omega_c$ and $d = 2l_B$ so that the radial variation of the potential (yellow curve in Fig. 4a) traces the observed distribution of the LL_0 subband. The same potential is applied to both models. The Landau level broadening is set as $\Gamma = 0.05\hbar\omega_c$, which is slightly better than the experimental energy resolution.

Important features in Fig. 4 are summarized as follows: (i) Discrete vertical ridges in the $n = 0$ and $n = 1$ Landau subbands, (ii) Splitting of the $n = 1$ Landau subband at the bottom of the potential, and (iii) Absence of nodal structure in the LDOS distributions.

As shown in Fig. S1a, the LDOS of the conventional electron system consists of a series of Landau subbands which are separated evenly in energy. The $n = 0$ Landau subband does not trace the potential curve but is shifted by $\hbar\omega_{c,C}/2$. The $n = 0$ Landau subband in Fig. S1a splits into a series of vertically extended ridges as similar to the case of the Dirac electron system (Fig. 4a). In the case of the conventional electron system, each ridge corresponds to a Landau orbit labelled by an orbital angular momentum $l_z\hbar$. Because Landau orbits with different l_z possess different guiding centre radii, the energy of each orbit changes in accordance with l_z in the presence of the potential variation $V(\mathbf{r})$. The energy separation between the adjacent orbits is large where the gradient of the potential is steep. The splitting become smaller with increasing number of the Landau level index n because the wider wave function distribution makes the effective potential gradient smaller [S3]. This phenomenon is an analogue of the Stark splitting induced by the potential gradient and commonly appears in both the Dirac and the conventional electron systems.

On the other hand, a remarkable difference is seen in the LDOS spectra at the bottom of the potential ($r = 0$); the LDOS spectrum splits into two peaks in the Dirac electron system (Fig. 4b), while no splitting occurs in the conventional electron system (Fig. S1b). In the case of the conventional electron system, the potential $V(\mathbf{r})$ does not mix the states with different orbital angular momentum $l_z\hbar$. Therefore the wave function $\Phi_{n,l_z}(r,\theta)$ in the presence of $V(\mathbf{r})$ is written as $\Phi_{n,l_z}(r,\theta) = \sum_{n'} c_{n,n'}\phi_{n',l_z}(r,\theta)$, where the set of functions $\{\phi_{n',l_z}(r,\theta)\}$ are the energy eigenstates for $V(\mathbf{r}) = 0$. Because $\phi_{n',l_z}(r = 0, \theta) = 0$ if $l_z \neq 0$ (see eq. (S5)), all the states with $l_z \neq 0$ do not have amplitudes at $r = 0$ ($\Phi_{n,l_z}(r = 0, \theta) = 0$
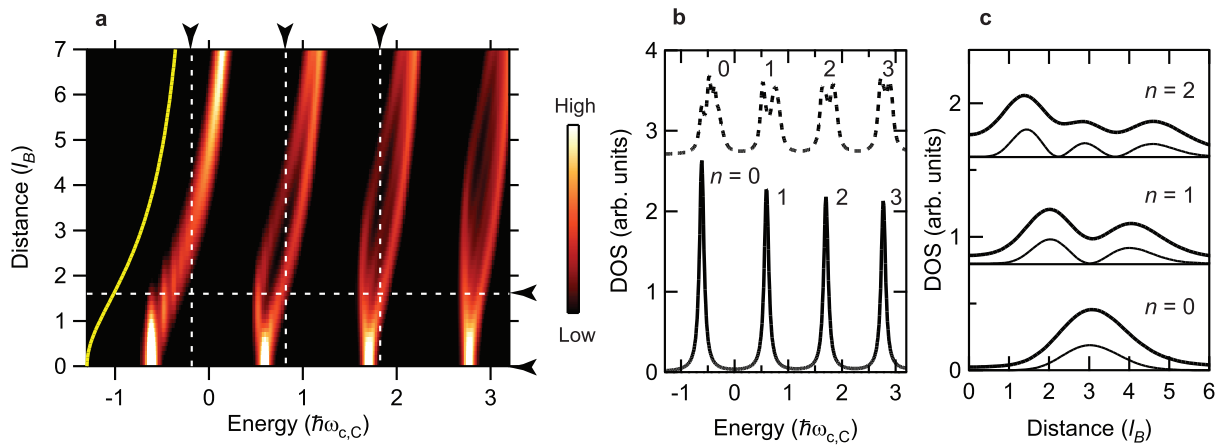
Figure S2: **Results of model calculations based on the conventional electron model with parabolic dispersion**. **a**, Intensity plot of calculated LDOS in the conventional electron system as a function of energy and distance from the bottom of the potential. The yellow curve denotes the radial variation of the potential used for the calculation. The energy is measured in units of $\hbar\omega_{c,C} = \frac{|e|B}{m^*}$ and the distance is measured in units of l_B. **b**, LDOS spectra obtained by taking horizontal line cuts at the representative points shown by horizontal arrows in **a**. (lower and upper traces correspond to distance $|r| = 0$ and $1.6l_B$, respectively.) Each curve is offset vertically for clarity. **c**, Thick solid curves represent internal structures of Landau orbits obtained by taking vertical line cuts at the representative energies shown by the vertical arrows in **a**. Thin solid curves show partial LDOS from the principal l_z states. Data for each n are offset vertically for clarity.

for $l_z \neq 0$). As a result, only a single state labelled by $l_z = 0$ has an amplitude at $r = 0$ in each Landau subband. Thus the LDOS does not split at the bottom of the potential in the case of the conventional electron system.

In the case of the Dirac electron system, the $\phi_{n,l_z=0}(r, \theta)$ function, which have non-zero amplitude at $r = 0$, can appear either in the upper component or in the lower component of the wave function $\boldsymbol{\Psi}_{n,j_z}(r, \theta)$, corresponding to the total angular momentum $j_z \hbar = +1/2\hbar$ and $-1/2\hbar$, respectively. Therefore the two energy eigenstates with $j_z = \pm 1/2$ have amplitudes at the bottom of the potential. Because these two states have different spatial extent, their energies are different in the presence of the potential, leading to the splitting of the LDOS accordingly. Thus, the splitting of the LDOS at the bottom of the potential is a direct consequence of the nature of the two-component wave functions.

Another difference between the conventional and the Dirac electron systems appear in the radial distribution of the LDOS. As shown in Fig. S1c, oscillations appear in the radial distribution of the LDOS of the conventional electron system, reflecting nodal structures in the amplitude of the wave functions. Because the number of the nodes in the wave function is equal to the Landau level index n, which is a topological number (Chern number), the oscillatory structure in the LDOS is believed to be robust in the conventional electron system [S4]. The appearance of the oscillations in the conventional electron system contrasts to the absence of the oscillation in the Dirac electron system as discussed in the main text (Fig. 4c).

2.3 Energy-resolved spin magnetization

We calculate the energy-resolved spin magnetization $m_i(E, \mathbf{r})$ $(i = x, y, z)$ using the model for the Dirac electron system. The energy-resolved spin magnetization is defined as

$$m_i(E, \mathbf{r}) = \frac{\hbar}{2} \sum_{n,j_z} \frac{\Gamma}{(E - E_{n,j_z})^2 + \Gamma^2} \times \boldsymbol{\Psi}^{\dagger}_{n,j_z}(r, \theta) \sigma_i \boldsymbol{\Psi}_{n,j_z}(r, \theta), \tag{S16}$$

where σ_i $(i = x, y, z)$ are Pauli matrices. Because j_z remains a good quantum number in the presence of the potential, the eigenstate wave functions in polar coordinates (r, θ) can be expressed in the separated-variable form of

$$\boldsymbol{\Psi}_{n,j_z}(r, \theta) = \begin{pmatrix} e^{i(l_z-1)\theta} f_{n,j_z}(r) \\ e^{il_z\theta} g_{n,j_z}(r) \end{pmatrix}, \tag{S17}$$

where $f_{n,j_z}(r)$ and $g_{n,j_z}(r)$ are real functions. Then the in-plane components (m_x, m_y) are calculated as

$$\begin{pmatrix} m_x \\ m_y \end{pmatrix} = \frac{\hbar}{2} \sum_{n,j_z} \frac{\Gamma}{(E - E_{n,j_z})^2 + \Gamma^2} \times 2 f_{n,j_z}(r) g_{n,j_z}(r) \begin{pmatrix} \cos\theta \\ \sin\theta \end{pmatrix}, \tag{S18}$$

and the out-of-plane component m_z is calculated as

$$m_z = \frac{\hbar}{2} \sum_{n,j_z} \frac{\Gamma}{(E - E_{n,j_z})^2 + \Gamma^2} \left(|f_{n,j_z}(r)|^2 - |g_{n,j_z}(r)|^2 \right). \tag{S19}$$

The calculated spatial distributions of the energy-resolved spin magnetization at three representative energies $(E = -0.67\hbar\omega_{\mathrm{c}}, 0.30\hbar\omega_{\mathrm{c}}$ and $0.71\hbar\omega_{\mathrm{c}})$ are shown in Figs. 4d-f. A data set with more energy points is presented in the Supplementary Movie 2.

3 Supplementary Movie 1

Evolution of localized Landau orbits with increasing energy. Conductance images taken at the same area as Fig. 2 at different energies are animated. The colour scale corresponds to a conductance range from 0.2 to 0.8 nS.

4 Supplementary Movie 2

Evolution of energy-resolved spin-magnetization distribution with increasing energy. Calculated distributions of the energy-resolved spin magnetization at different energies ranging from $E = -1.4 \hbar\omega_\mathrm{c}$ to 1.6 $\hbar\omega_\mathrm{c}$ are animated with an increment of 0.01 $\hbar\omega_\mathrm{c}$/frame. The in-plane components (m_x, m_y) are indicated by arrows and the out-of-plane component m_z is indicated by colours. Red (blue) represents positive (negative) magnetization. The line-cut at $y = 0$ is also shown above the panel.

References

[S1] Hanaguri, T. *et al.* T. Momentum-resolved Landau-level spectroscopy of Dirac surface state in Bi$_2$Se$_3$. *Phys. Rev. B* **82**, 081305(R) (2010).

[S2] Yoshioka, D. Local density of states around impurity in a strong magnetic field: I. Two-dimensional system with parabolic dispersion. *J. Phys. Soc. Jpn.* **76**, 024718 (2007).

[S3] Okada, Y. *et al.* Visualizing Landau levels of Dirac electrons in a one-dimensional potential. *Phys. Rev. Lett.* **109**, 166407 (2012).

[S4] Hashimoto, K. *et al.* Robust nodal structure of Landau level wave functions revealed by Fourier transform scanning tunneling spectroscopy. *Phys. Rev. Lett.* **109**, 116805 (2012).